nature energy

Article https://doi.org/10.1038/s41560-024-01614-7

Non-aqueous alkoxide-mediated electrochemical carbon capture

Received: 15 December 2023

Accepted: 25 July 2024

Andong Liu[1], Charles B. Musgrave III[2], Xing Li[1], William A. Goddard III[2] & Yayuan Liu[1]

Electrochemically mediated carbon capture utilizing redox-tunable organic sorbents has emerged as a promising strategy to mitigate anthropogenic carbon dioxide emissions. However, most reported systems are sensitive to molecular oxygen, severely limiting their application under ambient air conditions. Here we demonstrate an electrochemical carbon capture concept via non-aqueous proton-coupled electron transfer, where alkoxides are employed as the active sorbent while carbon dioxide absorption and desorption are modulated reversibly by the redox-tunable Brønsted basicity of certain organic molecules. Since all species involved in the process have outstanding oxygen stability and relatively low vapour pressure, our electrochemically mediated carbon capture mechanism intrinsically minimizes parasitic reactions and evaporative losses under aerobic conditions. Flow-based prototypes are demonstrated to operate efficiently in the presence of 20% oxygen under various practically relevant carbon dioxide feed concentrations, paving a way towards effective carbon capture driven by electrochemical stimuli.

Global warming caused by anthropogenic CO_2 emissions has become a major threat to the sustainability of our society[1]. In response to this crisis, development of techniques for capturing CO_2 from point or diffuse sources is urgently needed[2–4]. One major barrier to the incumbent wet chemical scrubbing methods is the high energy penalties of temperature-swing-based solvent regeneration[5,6]. Moreover, CO_2 separation using aqueous solvents tends to suffer from substantial evaporative loss, which is particularly problematic for direct air capture applications that require sizable solvent–air contact areas, limiting implementation in arid regions[7]. To lessen energy and evaporative losses, water-lean solvents are a recent impetus for carbon capture research[8,9]. Heldebrant et al. explored a class of CO_2-binding organic liquids (CO_2BOLs), typically consisting of a low-volatility alcohol and a non-nucleophilic superbase[10]. The alcohol can be deprotonated by the superbase to capture CO_2 as alkyl carbonates. The outstanding air stability, low volatility and low specific heat of CO_2BOLs endow them with better performance metrics than the industrial aqueous amine benchmark[11]. Nevertheless, current non-aqueous solvents for CO_2 chemisorption still rely on thermal regeneration, necessitating heat integration when retrofitting existing infrastructures and risking thermal degradation[12], which motivates fundamental research on CO_2 separation mechanisms driven by non-thermal stimuli.

Electrochemically mediated carbon capture (EMCC), which modulates CO_2 capture and release reversibly via electrochemical polarizations, is a promising alternative to thermochemical methods[13–16]. Using electricity as the driving force, EMCC can operate isothermally under ambient conditions, can be precisely controlled to minimize energy losses and can be modularly designed to adapt to the multiscale needs of carbon capture applications. Among EMCC pathways, utilizing redox-tunable Lewis bases as organic CO_2 carriers represents a well known strategy[17–20]. The reduction of redox-active carriers generates strong bases that form adducts with electrophilic CO_2, which can later be oxidized to release concentrated CO_2 while regenerating the sorbents (Fig. 1a). Despite their potential, obstacles remain for using redox-active CO_2 carriers in stringent scenarios such as direct air capture. Most of these sorbents degrade in aerobic conditions due to parasitic reactions between reduced species and molecular oxygen (O_2), which compete with CO_2 adduct formation and generate

---

[1]Department of Chemical and Biomolecular Engineering, Johns Hopkins University, Baltimore, MD, USA. [2]Materials and Process Simulation Center, California Institute of Technology, Pasadena, CA, USA. e-mail: yayuanliu@jhu.edu

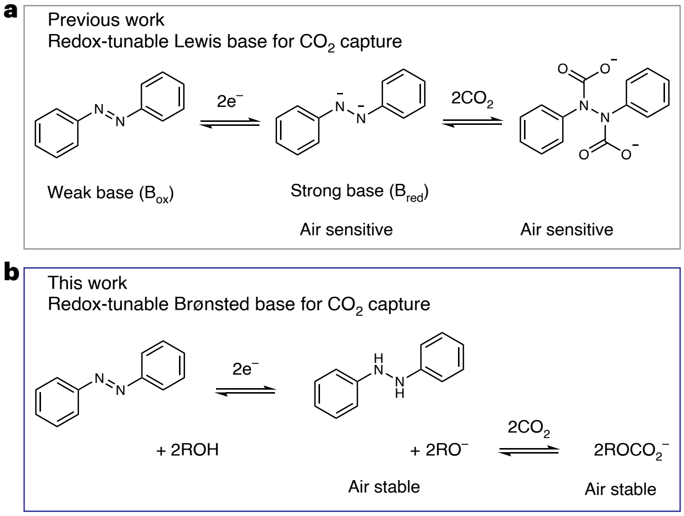

Fig. 1 | EMCC via non-aqueous PCET compared with previous redox-tunable CO_2 carrier. a, An EMCC mechanism based on redox-tunable Lewis bases as CO_2 carriers reported in previous studies[20], where CO_2 forms air-sensitive adducts with reduced Lewis bases. **b**, The EMCC mechanism developed in this work via non-aqueous PCET. Electroreduction of a redox-tunable Brønsted base deprotonates an alcohol, generating alkoxide as the sorbent for CO_2 capture. The non-aqueous PCET process enhances the robustness of the system against O_2 by affording air-stable products.

destructive superoxides[21]. To mitigate O_2 sensitivity, strategies such as molecular and electrolyte engineering have been implemented[22–24]. However, the possibility of stabilizing such EMCC systems under ambient air remains an open question.

Inspired by the ability of redox-tunable Lewis bases to serve as Brønsted bases in the presence of proton donors[25,26], herein we synergize the desirable attributes of non-aqueous solvents and electrochemical driving force to report a robust EMCC mechanism via non-aqueous proton-coupled electron transfer (PCET)[27,28]. Rather than forming CO_2 adducts, the redox-tunable Brønsted basicity of certain organic molecules is utilized to regulate CO_2 capture and release (Fig. 1b). Specifically, electroreduction increases the Brønsted basicity of the molecules to deprotonate alcohols and afford alkoxides, which absorb CO_2 as alkyl carbonates analogous to CO_2BOLs. In lieu of thermal energy input, the reduced Brønsted bases are electro-oxidized to release protons, regenerating the alcohols to desorb CO_2. The employment of low-volatility compounds minimizes evaporative losses and all active species involved are air stable, enhancing the resilience of the EMCC process. We screened various redox-tunable molecules, identifying azobenzene (AzB) as a promising candidate, and validated the mechanism by combined experimental and computational efforts. Linear alcohols were found to possess the most desirable properties among proton donors for EMCC via the PCET mechanism. Flow-based prototypes were evaluated in practically relevant scenarios with CO_2 concentrations ranging from 20% to 2,000 ppm, demonstrating high capacity, efficiency and stability with minimum performance loss in the presence of 20% O_2.

Examining appropriate redox-tunable Brønsted bases

The proposed EMCC mechanism relies on identifying redox-tunable Brønsted bases that can effectively deprotonate/activate alcohol-based CO_2 sorbents upon electroreduction. Ideal candidates should acquire at least one proton per electron transferred for maximized energy efficiency and have a relatively positive reduction potential to fit within the stability window of alcohols. Correspondingly, we examined the electrochemical behaviour of representative redox-tunable molecules with varying basicities, including quinones and compounds with sp^2 nitrogen moieties, in the presence of proton donors. *n*-Butanol was selected as a model proton donor given its common use in CO_2BOLs and relatively high boiling point (117.7 °C)[10,29]. The low volatility of the compounds was confirmed by measuring evaporative loss (Supplementary Fig. 1).

Figure 2 and Supplementary Fig. 2 summarize the cyclic voltammograms (CVs) of the selected molecules under different *n*-butanol concentrations. Without *n*-butanol, all molecules show two reversible voltammetric waves characteristic of stepwise two-electron transfer, in which the products of the first and second electron transfers are anion radicals and dianions, respectively. With increasing *n*-butanol concentrations, the molecules demonstrate modified electrochemical behaviours, indicating varying degrees of interactions with the proton donor.

Molecules with relatively low basicities, such as anthraquinone (AQ, Fig. 2a), present no evidence of PCET. With the introduction of *n*-butanol, the second redox wave shifts anodically without losing reversibility while the first redox wave remains unchanged, indicating that the AQ dianion can form only weak hydrogen-bonding complexes with *n*-butanol[30,31]. This is because the pK_a values of two-electron-reduced quinoids (7.84 for 9,10-anthracenediol, predicted value[32]) are only comparable to, if not lower than, typical alcohols used in CO_2BOLs (15.92 for *n*-butanol[33]), making them unable or kinetically sluggish to deprotonate alcohols.

Molecules featuring sp^2 nitrogen centres can possess much higher basicities than quinones, providing a stronger driving force to deprotonate alcohol. For molecules such as 4,4′-azopyridine (AzPy, Fig. 2b) and phenazine (PhN, Supplementary Fig. 2), the second redox wave shifts anodically with a gradual loss of reversibility with increasing *n*-butanol concentrations. This suggests that reduced AzPy and PhN afford strong hydrogen-bonding complexes with *n*-butanol, but proton transfer may only become dominant with sufficient excess of *n*-butanol[31].

We then turned to AzB, an even stronger base than AzPy and PhN (Fig. 2c). The half-wave potentials of AzB are more negative than those of other bases, confirming its higher basicity. With increasing *n*-butanol concentrations, the CVs are characterized by a gradual enhancement in the first reduction peak at the expense of the second redox wave. At an AzB to *n*-butanol molar ratio of 1:80, the current of the first reduction peak nearly doubles, indicating that the two electron transfer steps occur at almost the same potential. This suggests that the AzB anion radical is basic enough to deprotonate *n*-butanol[34], corresponding to our desired PCET process where one proton is translocated per electron transfer. Moreover, a new oxidation peak more positive than the original one appears and shifts anodically with increasing *n*-butanol concentrations, consistent with hydrazobenzene (HAzB) formation, which requires extra energy to break the N–H bond.

To corroborate our results, density functional theory (DFT) calculations were performed to interrogate the thermodynamics of the non-aqueous PCET process (Supplementary Table 1)[20]. The Gibbs free energies of the first PCET reaction (protonation of the radical anion) are +0.15, −0.13, −0.75 and −1.02 eV for AQ, AzPy, PhN and AzB, respectively, and the values for the second PCET reaction (protonation of the singly protonated anion) are −0.05, −0.5, −1.34 and −1.45 eV for AQ, AzPy, PhN and AzB, respectively. The calculations are consistent with our experimental observation that weaker electrogenerated bases present higher barriers to protonation.

The CV measurements provide molecular-level guidance to the selection of redox-tunable Brønsted bases for EMCC via non-aqueous PCET. Given that strong basicity facilitates efficient deprotonation of alcohols upon electroreduction, AzB was chosen for our subsequent exploration. Note that the potential of AzB fits within the electrochemical stability window of *n*-butanol and dimethylsulfoxide (DMSO). Moreover, negligible reduction current is observed within the stability window under CO_2, eliminating the possibility of CO_2 reduction during capture–release cycles (Supplementary Fig. 3).

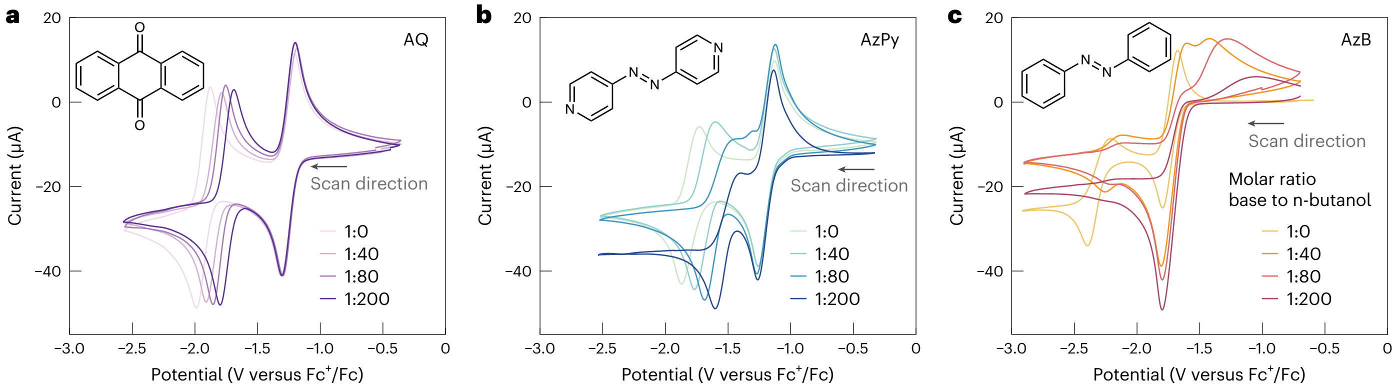

Fig. 2 | Interaction between *n*-butanol and different redox-tunable base molecules. a–**c**, CVs of AQ (**a**), 4,4′-AzPy (**b**) and AzB (**c**) in the presence of varying *n*-butanol additive concentrations. The CVs were collected under nitrogen at a scan rate of 20 mV s^{-1} using 10 mM redox-tunable base solubilized in DMSO with 0.1 M tetrabutylammonium hexafluorophosphate (NBu_4PF_6) as the supporting salt. The legends denote the redox-tunable base to *n*-butanol molar ratios. A 3 mm glassy carbon, a platinum wire and a silver wire were used as the working, counter- and reference electrodes, respectively. Fc was used as an internal reference.

Chemical validation of the alkoxide-mediated EMCC mechanism

The initial electrochemical findings encouraged us to unambiguously validate the feasibility of EMCC via non-aqueous PCET. We first quantified the CO_2 capture–release behaviour of *n*-butanol induced by chemical deprotonation–protonation. The experimental set-up involves continuously purging a septum-sealed vial with CO_2 and monitoring the outlet CO_2 concentration (Fig. 3a; referred to as injection experiment hereafter). When a known amount of chemically prepared *n*-butoxide was injected into the vial, the CO_2 concentration dropped immediately due to the acid–base reaction with CO_2 (Fig. 3b). Afterwards, 1 M H_2SO_4 was added to simulate the increased proton concentration upon electro-oxidation of the redox-tunable Brønsted base. A sharp rise in CO_2 concentration was observed, consistent with *n*-butanol regeneration and CO_2 release. Integration of the CO_2 concentration curve indicates that 93.3% of *n*-butoxide reacted with CO_2 and 92.6% of captured CO_2 was released, confirming an effective and highly reversible CO_2 capture–release process mediated by *n*-butoxide.

Proton nuclear magnetic resonance (^{1}H NMR) spectra at each stage of the capture–release cycle were monitored (Fig. 3c). The proton in the hydroxyl group of *n*-butanol (4.50 ppm) disappeared after reacting with sodium hydride and reappeared after adding H_2SO_4. Integration of the peaks shows a 1:2 ratio between the hydroxyl proton and protons on the α carbon (3.38 ppm), confirming the full regeneration of *n*-butanol. This evidence supports the reversible protonation–deprotonation of *n*-butanol and our postulation that *n*-butoxide can act as the active intermediate to capture CO_2.

White precipitates formed in the injection experiment when purging CO_2 into *n*-butoxide solution due to the formation of the sodium salt of *n*-butyl carbonate, which can be dissolved by adding 15-crown-5 to chelate sodium ion (Supplementary Fig. 4)[35]. Compared with *n*-butanol, the Fourier transform infrared (FTIR, Fig. 3d) spectrum of the precipitates shows three new peaks. The peaks at 1,336 and 1,423 cm^{-1} correspond to C=O symmetrical stretching, and that at 1,609 cm^{-1} corresponds to asymmetrical stretching of the carboxylic group[36,37]. These peaks strongly indicate the formation of *n*-butyl carbonate. Notably, the FTIR spectrum remains unchanged in ambient air after >6 h, confirming the high air stability of *n*-butyl carbonate.

To verify the reversible PCET reaction of AzB, we conducted bulk electrolysis of AzB (Supplementary Fig. 5). The ^{1}H NMR spectrum of pristine AzB shows two multiplet peaks at 7.59 and 7.90 ppm (Fig. 3e and Supplementary Fig. 6). After electroreduction in the presence of *n*-butanol under nitrogen, protons on the benzene ring moved to lower chemical shifts and a new peak corresponding to protons on *sp*^{3} nitrogen appeared at 7.60 ppm, indicating HAzB formation. Correspondingly, the colour of the solution changed from orange to pale yellow. The Tyndall effect was observed when the reduced solution was purged with CO_2, corroborating the formation of *n*-butyl carbonate colloids. The phenomena strongly support our proposed EMCC mechanism: that reduced AzB can deprotonate *n*-butanol to afford *n*-butoxide for CO_2 capture. Since alkoxide undergoes fast proton exchange with alcohol and alkyl carbonate precipitates out of the solution, NMR peaks of these two species were not readily observable in the reduced samples. Importantly, on the basis of the ^{1}H NMR spectra, electro-oxidation of HAzB with *n*-butyl carbonate regenerated AzB. The solution returned to orange colour with the disappearance of colloidal *n*-butyl carbonate. Bulk electrolysis also confirmed that weaker redox-tunable bases cannot effectively undergo PCET with *n*-butanol (Supplementary Fig. 7).

Excitingly, HAzB possesses outstanding stability in oxidative environments. The NMR spectrum of HAzB solution purged with pure O_2 for 1 h shows negligible changes when compared with the pristine compound (Supplementary Fig. 8), outperforming the state-of-the-art redox-active CO_2 carrier[20]. Specifically, we recently reported AzPy as a redox-tunable Lewis base for EMCC that is relatively stable against O_2 due to its more positive redox potential than oxygen reduction. The EMCC prototype using AzPy performed well under 15% CO_2 with 5% O_2. Nevertheless, the colourless AzPy–CO_2 adduct still reverted to the orange colour of AzPy after an hour of air exposure (Supplementary Fig. 9). Therefore, the high air stability of HAzB and alkyl carbonates offers a promising solution to the oxygen sensitivity issue plaguing many previous EMCC processes.

Optimizing alkoxide- and phenoxide-based CO_2 sorbent

Pronounced efforts have been made to explore alkoxides and phenoxides as CO_2 absorbents, prompting us to optimize our sorbent chemistry[35,38]. An ideal sorbent should efficiently transfer protons to reduced AzB and exhibit high CO_2 affinity upon deprotonation. However, these two properties can be limited by the intrinsic trade-off between the acidity of a sorbent molecule and the basicity of its conjugated base. We compared sorbents from three molecular families (linear alcohols and 4-substituted and 2,6-substituted phenols) to elucidate the underlying structure–property relationships.

We first evaluated the facileness of alcohol/phenol deprotonation by reduced AzB. We used the ratio between the integrated CV areas of the first and second reduction peaks of AzB in the presence of alcohol/phenol as a measure of deprotonation propensity (Supplementary Figs. 10–13). All three sorbent families exhibit a linear relationship between deprotonation propensity and pK_a, yet the

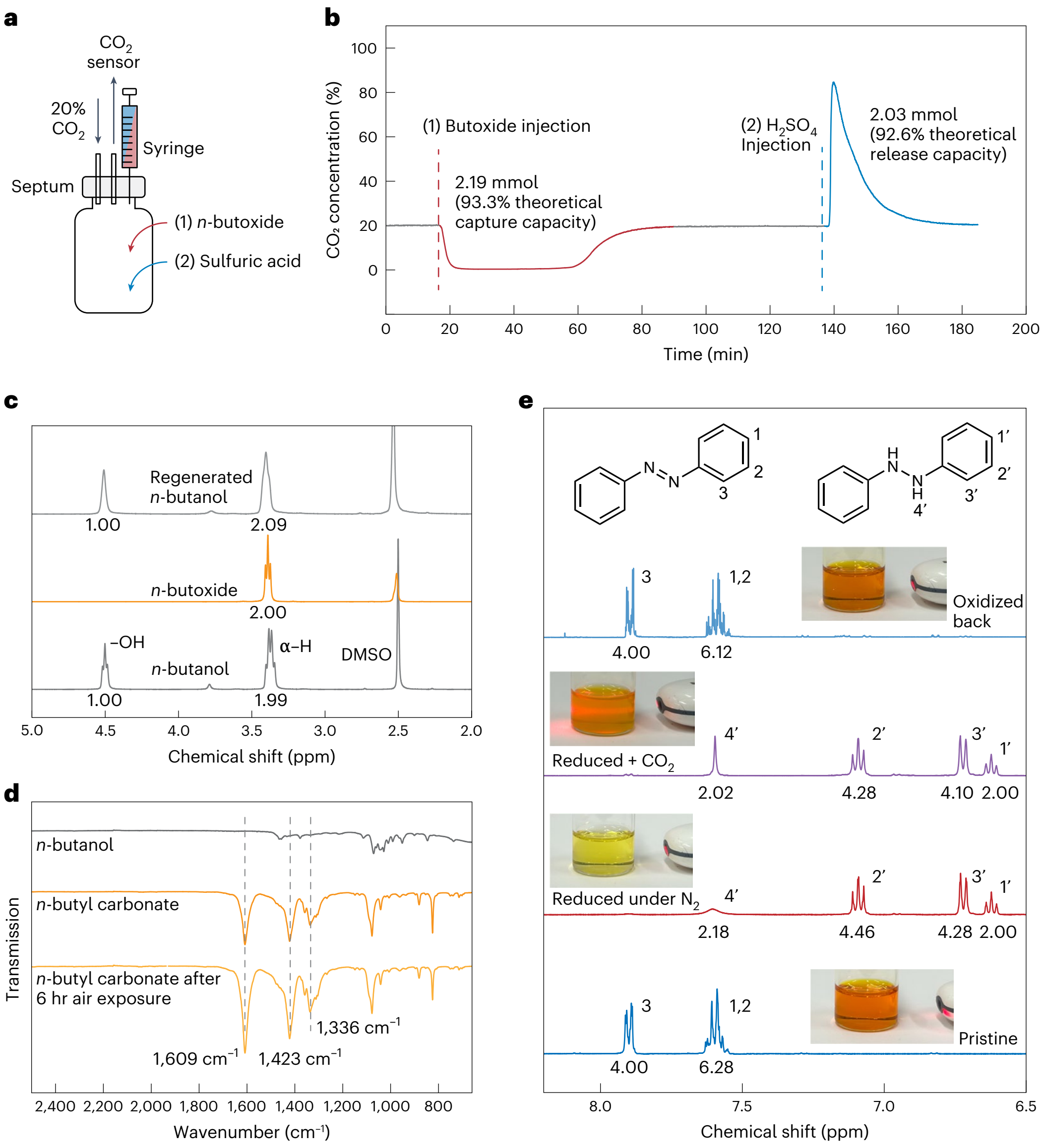

Fig. 3 | Chemical validation of the non-aqueous alkoxide-mediated EMCC mechanism. a, Schematic of the injection experiment. The septum-sealed vial was continuously purged with 20% CO_2 at a constant flow rate. The outlet CO_2 concentration was monitored using an infrared-based sensor after injecting the corresponding chemicals into the vial. **b**, CO_2 concentration reading curve as a function of time upon *n*-butoxide and H_2SO_4 addition and the corresponding quantification of the amount of CO_2 captured and released. **c,** ^1H NMR spectra of pristine *n*-butanol in DMSO (bottom), *n*-butanol reacted with sodium hydride (middle) and *n*-butanol regenerated with H_2SO_4 (top). **d**, FTIR spectra of pristine *n*-butanol (top), just prepared *n*-butyl carbonate (middle) and *n*-butyl carbonate exposed to ambient air for 6 h (bottom). **e**, Zoomed-in ^1H NMR spectra between 8.25 and 6.50 ppm of AzB electrolyte solution at different stages of a redox cycle. The full spectra are shown in Supplementary Fig. 6. The insets show the colour of the solution. A laser pointer was used to observe the Tyndall effect due to the formation of colloidal *n*-butyl carbonate. 3 ml of 0.1 M AzB in non-deuterated DMSO was electrochemically reduced or oxidized in the presence of 4 M *n*-butanol under nitrogen or CO_2, with 0.2 M LiTFSI as the supporting salt. NMR samples were prepared by mixing 0.5 ml of electrolyte solution with 0.3 ml of deuterated DMSO.

strength of the correlation varies (Fig. 4a). The deprotonation propensity of 4-substituted phenols drops substantially with only a slight increase in pK_a, while the scaling is much weaker for linear alcohols and 2,6-substituted phenols. ^1H NMR spectra of AzB after bulk electrolysis and the corresponding electrochemical polarization curves suggest that ~50% and ~88% of reduced AzB is protonated by *n*-butanol and phenol, respectively, confirming that sorbents with lower pK_a have a higher deprotonation propensity (Supplementary Figs. 14 and 15).

We then quantified the CO_2 affinity of alkoxides/phenoxides through injection experiments. We define CO_2 capture efficiency as the ratio between the actual amount of CO_2 captured and the theoretical capacity, assuming that alkoxides/phenoxides react with CO_2 at a 1:1 stoichiometry. Sorbent with higher capture efficiency suggests greater CO_2 affinity (Fig. 4b and Supplementary Table 2). As expected, CO_2 affinity correlates positively with pK_a. Again, the scaling relationship is much weaker for linear alkoxides than for 4-substituted phenoxides, such that the former consistently show a high capture efficiency above 65%. Compared with other molecules of similar pK_a, 2,6-substituted phenoxides show much lower capture efficiency, probably caused by the *ortho* substitutions that sterically hinder CO_2 binding.

From the discussion above, linear alcohols are less sensitive towards the scaling relationship between deprotonation ability and CO_2 capture efficiency (Supplementary Fig. 16), making them well suited as platform sorbents for EMCC via non-aqueous PCET. Their high (electro)chemical stability further supports this selection (Fig. 4c,d). Linear alcohols exhibit stability across a broad potential range, whereas phenols show

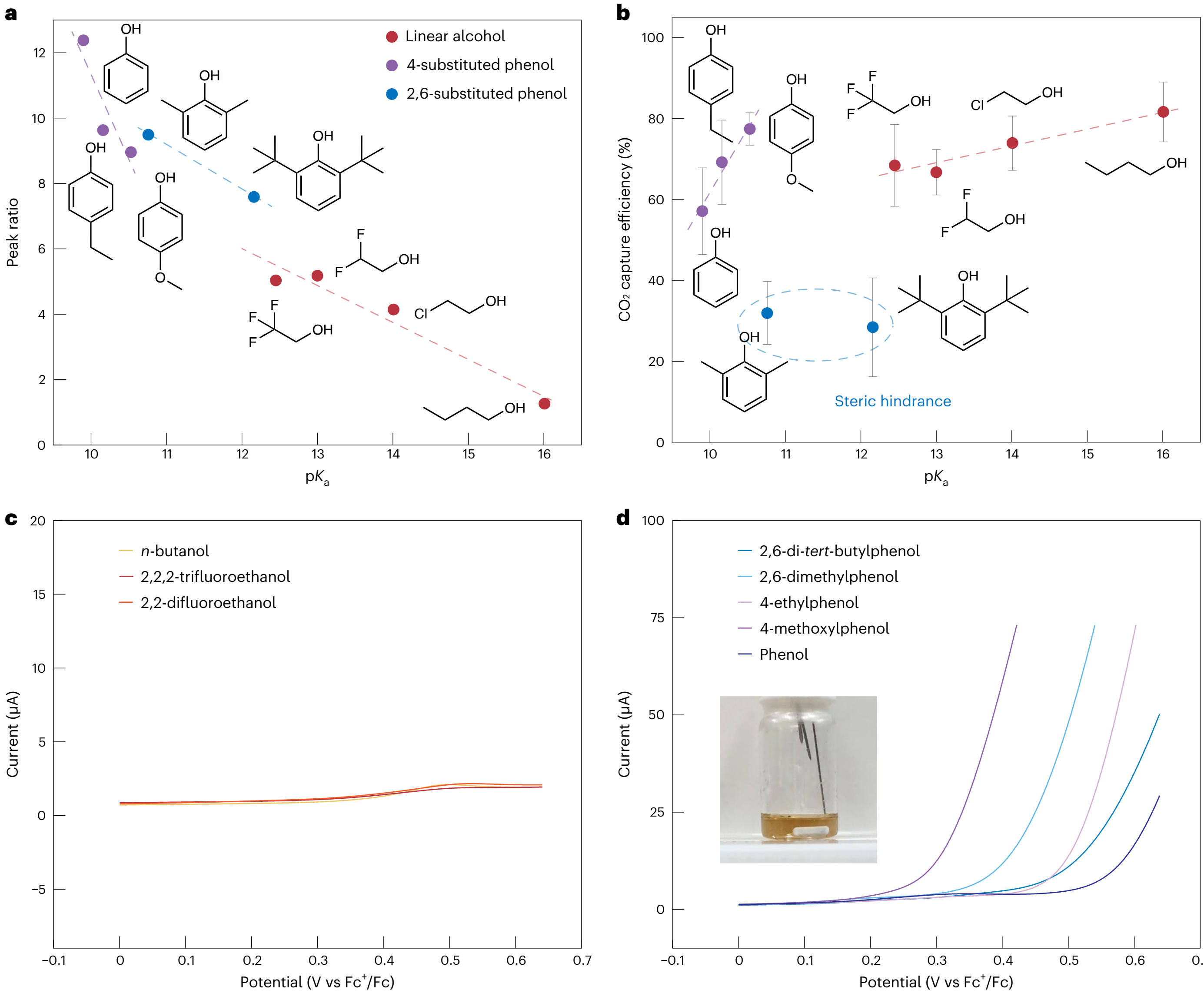

Fig. 4 | Sorbent optimization. a, Correlation between the deprotonation propensity of linear alcohols or phenols and their pK_a. Given the fact that PCET has a substantial impact on the CV behaviour of AzB, the ratio between the integrated areas of the first and second reduction peaks of AzB in the presence of alcohol/phenol molecules was employed to measure the sorbents' propensity towards deprotonation. A higher peak ratio indicates a higher deprotonation propensity. The trend lines are guides to the eye. **b**, Correlation between the CO_2 affinity of alkoxides or phenoxides and their pK_a (data points plotted are the mean values, and error bars represent the maximum and minimum values from three separate measurements). **c**,**d**, CVs of linear alcohols (**c**) and phenols (**d**) showing their electrochemical stability windows. The CVs were measured under nitrogen at a scan rate of 20 mV s^{-1} using 0.1 M sorbent dissolved in DMSO with 0.1 M NBu_4PF_6 as the supporting salt. Inset: the colour of deprotonated 4-methoxylphenol after being exposed to ambient air.

early onsets of oxidative decomposition, posing risks of parasitic reactions during CO_2 release. Additionally, phenoxides can be vulnerable to O_2, as the colourless 4-methoxylphenolate solution quickly turned into brownish benzoquinone upon air exposure (Fig. 4d inset). Thus, we chose linear alcohols as sorbents for subsequent EMCC tests.

Mechanistic investigation of EMCC via non-aqueous PCET

The coexistence of redox-tunable base, proton donor and CO_2 in our electrochemical environment raises questions about the possible competition between two EMCC pathways in which AzB serves as either a Brønsted base (PCET mechanism) or a Lewis base (direct CO_2 capture mechanism). DFT calculations were conducted to elucidate the thermodynamics of the two pathways. The free-energy changes of each elementary step and a full reaction scheme are shown in Fig. 5 and Supplementary Fig. 17, respectively. The hydrogen-bonding effect of *n*-butanol was not considered as it does not affect the thermodynamics of the process (Supplementary Fig. 18).

We first consider the use of bulky, coordination-inhibited NBu_4^+ as the supporting cation, as in our CV experiments (Fig. 5a, blue lines). The reaction landscape suggests that the PCET pathway is thermodynamically favoured, with potential kinetic competition from the direct CO_2 capture mechanism. Specifically, the direct CO_2 capture mechanism is energetically downhill throughout the reaction, whereas there is a slight energy barrier for deprotonation of *n*-butanol by the AzB radical anion (0.58 eV) in the PCET mechanism. Nonetheless, the total free-energy change of the PCET process (−5.48 eV) is more negative than that of CO_2 adduct formation (−5.08 eV), as the strong interaction between *n*-butoxide and CO_2 (−1.27 eV per CO_2) contributes an appreciable thermodynamic driving force to the former mechanism.

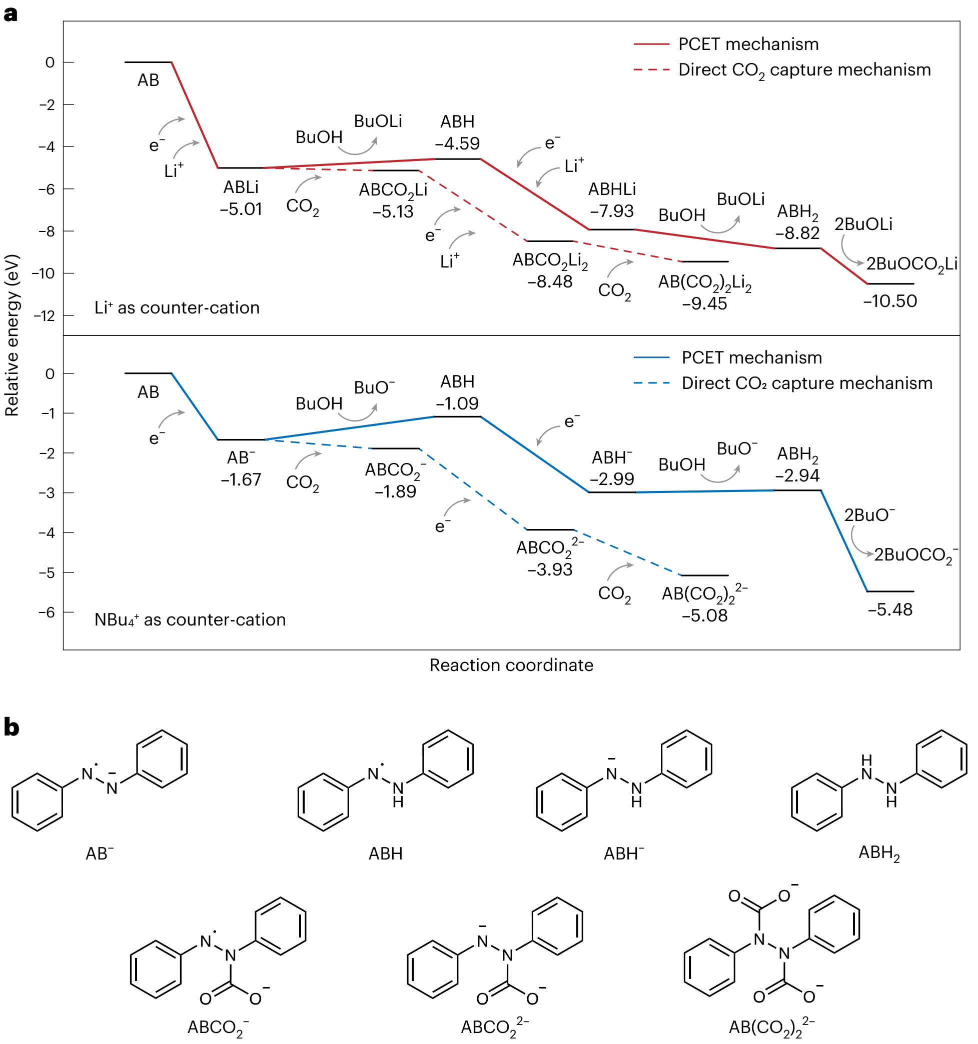

Fig. 5 | Mechanistic investigation of EMCC pathways. a, DFT-predicted free-energy landscape for the EMCC process. Two possible mechanisms are considered, in which AzB serves as either a redox-tunable Brønsted base (PCET mechanism) or a redox-tunable Lewis base (direct CO_2 capture mechanism). Two supporting electrolyte cations are considered: the strongly coordinating Li^+ and the weakly coordinating NBu_4^+. The free-energy change for each reaction step was computed as the sum of the product free energies minus the sum of the reactant free energies of that particular reaction step. For the chemical reaction steps (proton transfer steps or CO_2 binding steps), the free energies of *n*-butanol and CO_2 were included in the calculation. **b**, Chemical structures of the intermediates considered in **a**.

We further consider the case when a strongly coordinating cation (Li^+) is employed as the counterion, which is relevant to bulk electrolysis and subsequent prototype testing (Fig. 5a, red lines). Changing cation identity does not alter our conclusion that PCET is the thermodynamically favourable pathway. Importantly, the coordinating effect of Li^+ enlarges the overall energy difference between the two mechanisms from 0.40 eV to 1.05 eV, and the energy barrier for the first *n*-butanol deprotonation step drops to 0.42 eV.

We measured the forward rate constant (k_f) of the protonation and CO_2 complexation reactions of the AzB radical anion (Supplementary Fig. 19; see Supplementary Note 1 for details). The k_f for direct CO_2 binding (32.3 s^{-1}) is nearly ten times that of protonation by *n*-butanol (3.51 s^{-1}), aligning with DFT predictions of a slight kinetic barrier in the first PCET reaction. Subsequently, we verified the most thermodynamically stable carbon capture product via bulk electrolysis with the coexistence of CO_2 and *n*-butanol. The NMR spectrum indicates that HAzB is the only product (Supplementary Fig. 20), agreeing with DFT results that the PCET mechanism is thermodynamically dominant. Note that during practical operation (Supplementary Fig. 21) active carbon capture species are generated inside the electrochemical cell without exposure to the CO_2-containing gas feed. Given the much lower CO_2 concentration in the electrolyte when compared with *n*-butanol, the formation of *n*-butoxide and HAzB will be both kinetically and thermodynamically favourable. This ensures that all non-transient species involved in the process have good O_2 stability for efficient EMCC.

Flow-based EMCC prototype

With optimized chemistry, we constructed a flow-based prototype to evaluate our EMCC mechanism across various scenarios (see Supplementary Table 3 for testing parameters). The prototype comprised a sorbent tank and a counter-electrolyte tank[19,20]. The sorbent electrolyte contained AzB and *n*-butanol in DMSO with lithium bis(trifluoromethanesulfonyl)imide (LiTFSI) as the supporting salt. The counter-electrolyte replaced AzB with ferrocene (Fc). Electrolytes were circulated through an electrochemical flow cell. A constant CO_2 flow was introduced into the sorbent tank, and the outlet concentration was measured continuously (Supplementary Fig. 22).

Figure 6a shows the cyclic capture–release behaviour of the prototype at a 16% CO_2 feed (balanced by nitrogen). CO_2 reading curves of selected cycles are overlaid in Fig. 6b, and the cumulative amounts of

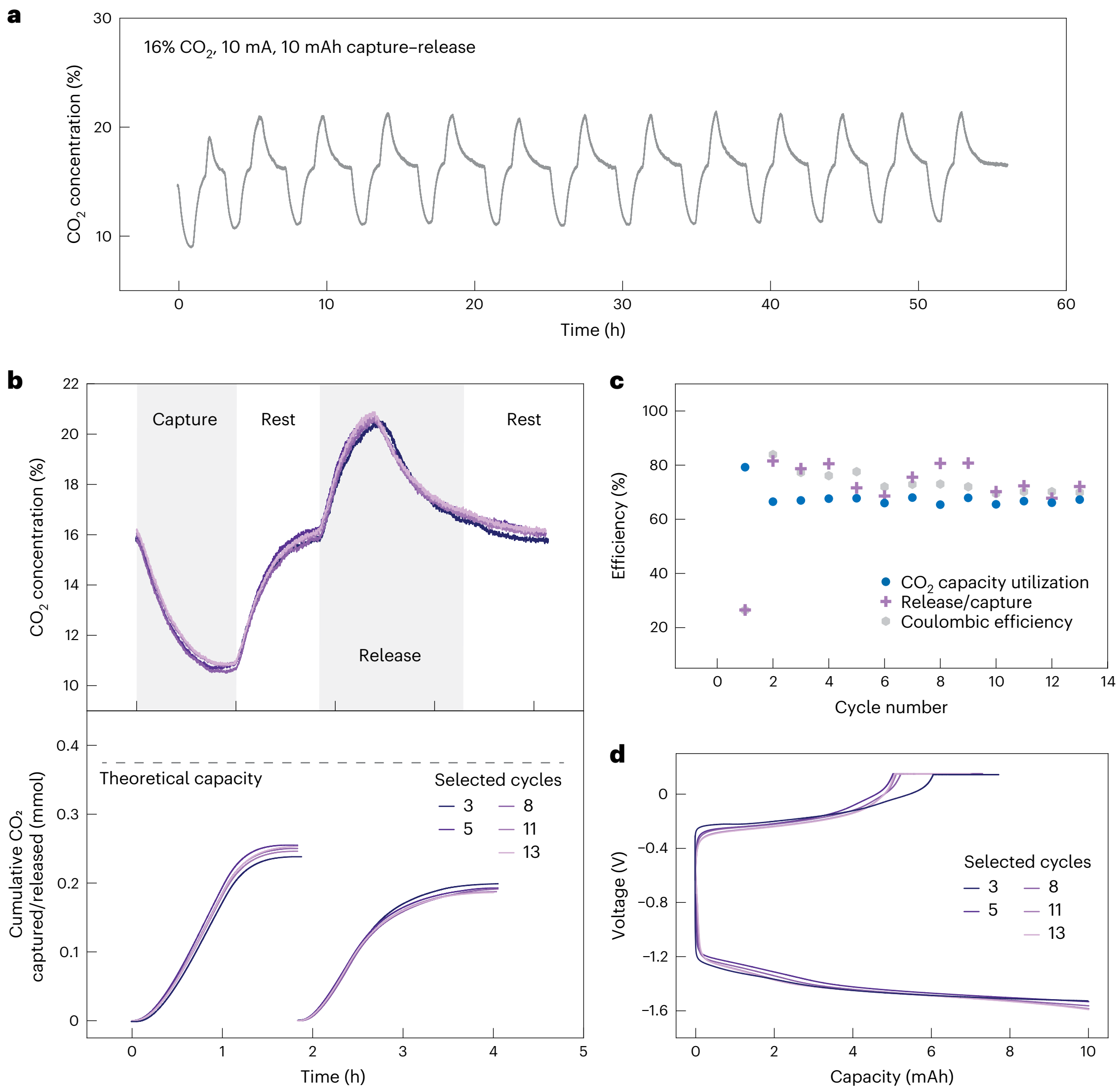

Fig. 6 | EMCC prototype performance with 16% CO_2 feed. a, CO_2 reading at the exit of the sorbent tank over 13 repeating capture–release cycles for ~55 h of operation. **b**, CO_2 reading of selected capture–release cycles, with the cumulative amount of CO_2 captured/released in each cycle relative to the theoretical capacity. For CO_2 capture, AzB was reduced at 10 mA for 60 min followed by a 50 min rest. For CO_2 release, HAzB was oxidized at 10 mA to 0.15 V, followed by a constant voltage hold, and finally rested for 45 min. **c**, CO_2 capacity utilization efficiency, release/capture efficiency and Coulombic efficiency of the system. **d**, Voltage–capacity curves for selected capture–release cycles. 7 ml of sorbent electrolyte and 12 ml of counter-electrolyte were used. The sorbent tank was purged with 16% CO_2 at a flow rate of 2 standard cubic centimetres per minute (sccm).

CO_2 captured/released can be obtained by integrating these curves. For each cycle, AzB was first reduced to generate *n*-butoxide, during which the drop in outlet CO_2 concentration indicated carbon capture. The current was then set to zero, allowing the CO_2 reading to return to baseline as *n*-butoxide fully reacted with CO_2 and the headspace reached equilibrium with the electrolyte. Subsequently, HAzB was oxidized following a constant current–constant voltage protocol, and the increase in CO_2 concentration above baseline indicated CO_2 release. Afterwards, the current was set to zero again to ensure complete release of the oversaturated CO_2 from the electrolyte. The prototype demonstrated stable operation for over 13 cycles (55 h) without obvious decay.

Figure 6c summarizes three key metrics commonly used for evaluating EMCC performance. The CO_2 capacity utilization efficiency, defined as the amount of CO_2 captured relative to the theoretical value (assuming one CO_2 per electron), averaged at 67%. We noticed an appreciable amount of Fc crossover into the sorbent electrolyte during cycling, which can chemically oxidize HAzB or participate in charge transfer with the electrode, leading to capacity utilization inefficiency. To evaluate the reversibility of the system, we define the ratio of the amount of CO_2 released to that captured as the release/capture efficiency and the ratio of the electrochemical oxidation capacity to reduction capacity as the Coulombic efficiency. These two values were averaged to be 74.4% and 73.1%, respectively. The proximity of the two values suggests negligible parasitic reactions in the process and that one electron transfer can successfully induce one CO_2 release.

To investigate the reason behind the less-than-unity efficiencies, NMR spectra of the sorbent electrolyte after cycling are collected (Supplementary Fig. 23). Both *n*-butanol and AzB retained their structural integrity, ruling out chemical degradations as the cause. HAzB residual peaks remained after cycling, suggesting that one contributing factor to the inefficiencies was our constant current–constant voltage protocol, where HAzB was not fully oxidized back within a reasonable timescale. A pronounced Fc peak was observed after cycling, indicating a rather severe Fc/Fc^+ crossover that hinders the reversibility of the system. Since the degree of crossover is time dependent, decreasing the rest time between capture and release can help mitigate this issue

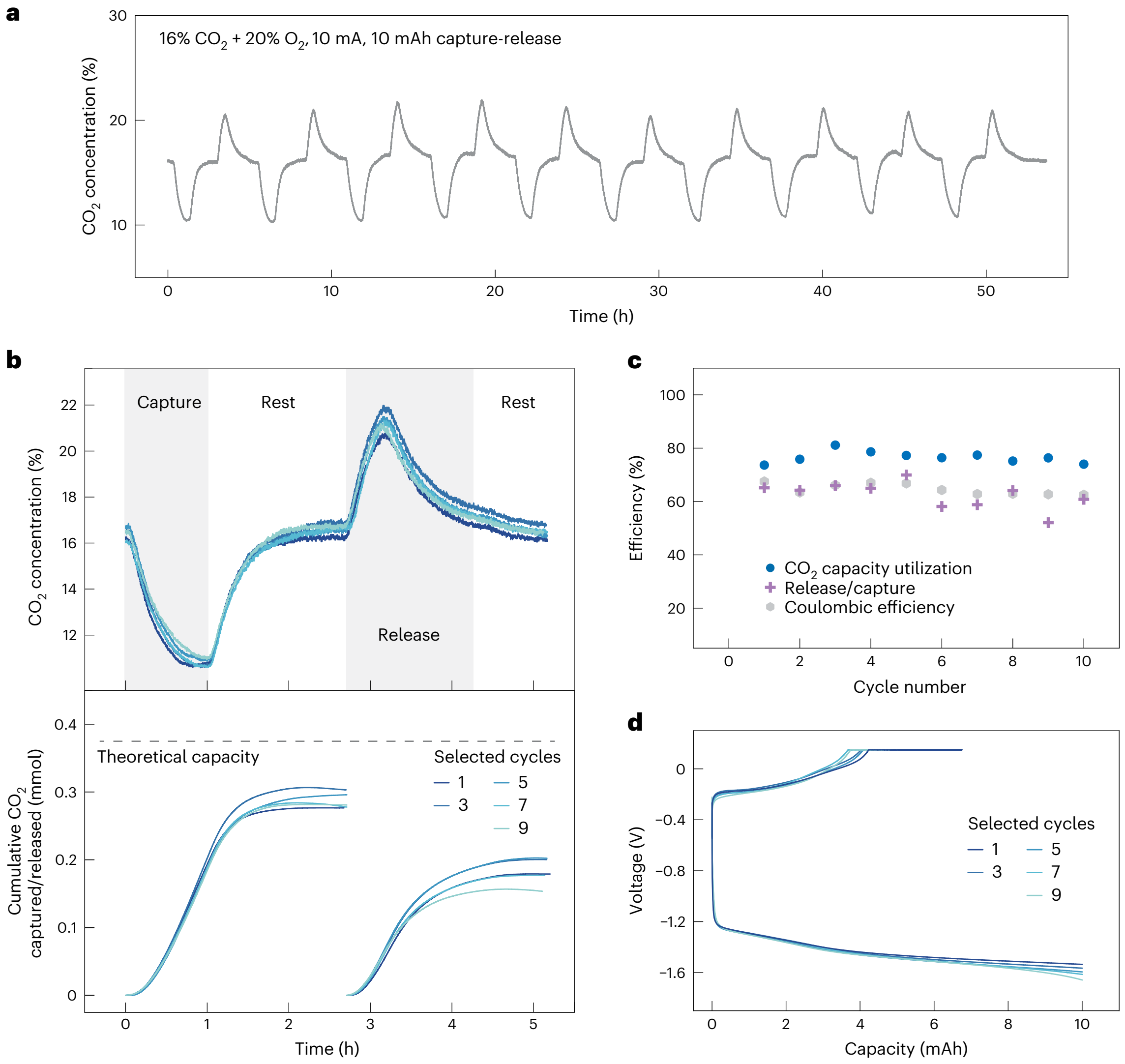

Fig. 7 | EMCC prototype performance with simulated flue gas. a, CO_2 reading at the exit of the sorbent tank over 10 repeating capture–release cycles for ~55 h of operation. **b**, The CO_2 reading of selected capture–release cycles, with the cumulative amount of CO_2 captured/released in each cycle relative to the theoretical capacity. For CO_2 capture, AzB was reduced at 10 mA for 60 min followed by a 100 min rest. For CO_2 release, HAzB was oxidized at 10 mA to 0.15 V, followed by a constant voltage hold, and finally rested for 45 min. **c**, The CO_2 capacity utilization efficiency, release/capture efficiency and Coulombic efficiency of the system. **d**, Voltage–capacity curves for selected capture–release cycles. 7 ml of sorbent electrolyte and 12 ml of counter-electrolyte were used. The sorbent tank was purged with 16% CO_2 at a flow rate of 2 sccm, and the solution was purged with 20% O_2 for 30 min during the rest period after capture.

(Supplementary Fig. 24). In actual practice, the rest step is unnecessary such that higher efficiencies can be expected.

The oxidation/reduction voltage profiles are shown in Fig. 6d. By integrating the voltage–capacity curve and normalizing to the amount of CO_2 captured, the average energy consumption under 16% CO_2 was ~177.1 kJ per mol CO_2 (Supplementary Table 4; CO_2 capture rate is summarized in Supplementary Table 5 and Supplementary Note 2). The energy consumption can be attributed to two factors. First, electrochemical impedance spectroscopy implies a relatively high ohmic resistance from the non-aqueous electrolyte and Nafion membrane (Supplementary Fig. 25). Second, the chemical stability of HAzB and the strong binding between Li^+ and *n*-butyl carbonate lead to a relatively high oxidation energy barrier. On the basis of the onset potential gap between oxidation and reduction (Supplementary Fig. 26), the minimum theoretical energy requirement is 80.1 kJ per mol CO_2. Our prototype is only a proof of concept for the EMCC mechanism. Future optimizations at the material and device levels, such as synthesizing membranes with high ionic conductivity in non-aqueous electrolytes[39] and developing electrode/electrolyte modification to promote charge transfer[40], can improve the energetics of the system.

The robustness of our EMCC system against O_2 impurity was demonstrated by co-feeding 20% O_2 into the sorbent tank (Fig. 7; simulated flue gas). The system maintained high stability over repeated capture–release cycles, with an uncompromised CO_2 capacity utilization efficiency (averaging ~75%) when compared with that without O_2 and an average energetics of ~170.1 kJ per mol CO_2. This demonstration of high-efficiency operation under ambient O_2 conditions is outstanding when compared with previous EMCC studies involving redox-active organic molecules (Supplementary Table 6)[20,23,41–44]. In contrast, without *n*-butanol, the presence of O_2 caused a rapid performance decay within a few cycles (Supplementary Fig. 27).

We further evaluated the prototype under more stringent feed conditions relevant to practical applications (Fig. 8, Supplementary Figs. 28–30 and Supplementary Table 3). The degree of CO_2 removal is critical for point-source carbon capture. Correspondingly, we demonstrated the capability of our EMCC mechanism in deep CO_2 removal by employing a higher operating current and a lower gas

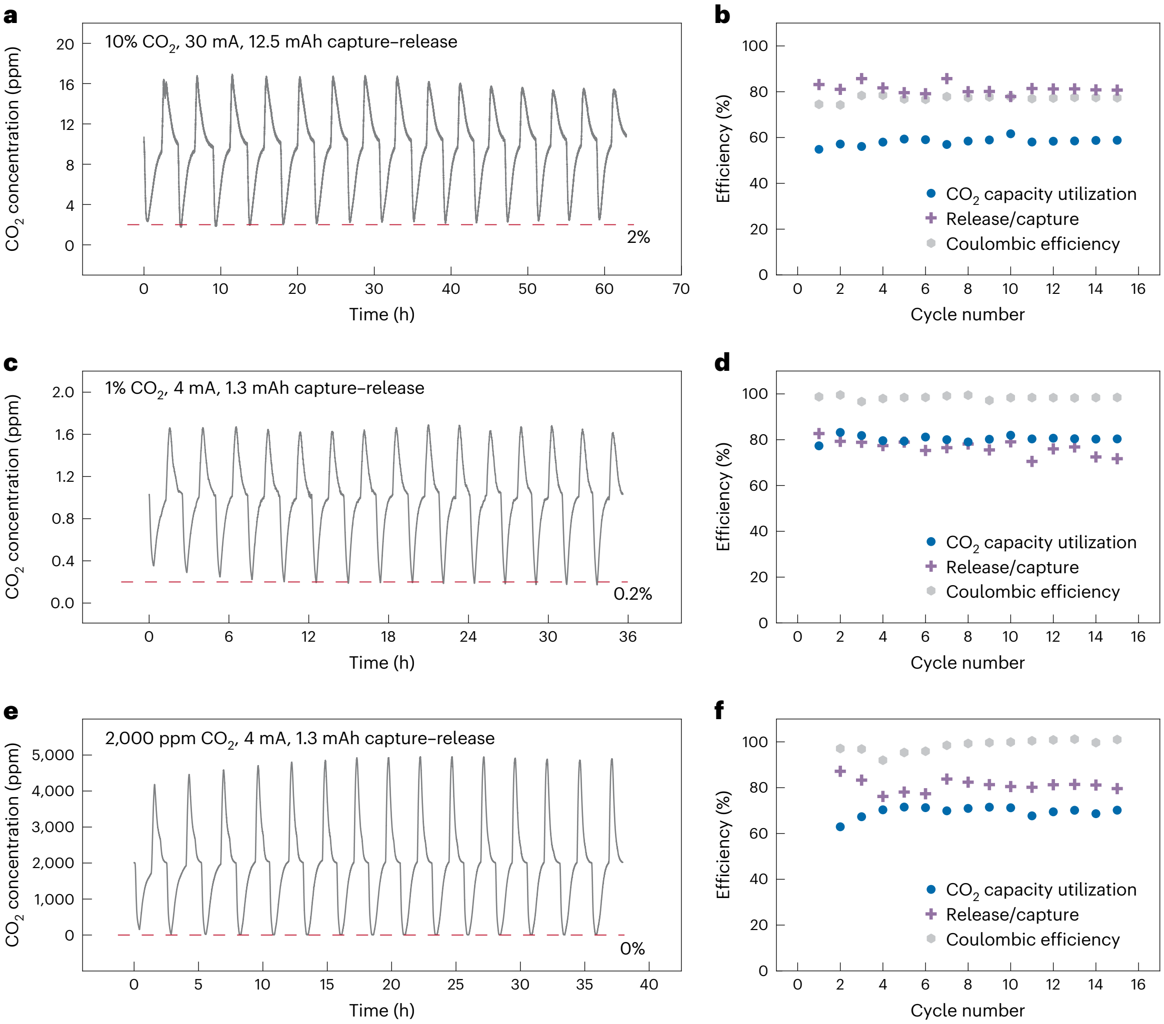

Fig. 8 | EMCC prototype performance in practically relevant scenarios. **a**,**c**,**e**, CO_2 reading at the exit of the sorbent tank over 15 repeating capture–release cycles under 10% (**a**), 1% (**c**) and 2,000 ppm (**e**) CO_2. **b**,**d**,**f**, The CO_2 capacity utilization efficiency, release/capture efficiency and Coulombic efficiency of the system under 10% (**b**), 1% (**d**) and 2,000 ppm (**f**) CO_2. 10 ml of sorbent electrolyte was used for the 10% CO_2 feed, and 7 ml of sorbent electrolyte was used for the 1% and 2,000 ppm CO_2 feeds. The gas flow rates were 1.5, 4 and 10 sccm, respectively, for 10%, 1% and 2,000 ppm feeds. 13 ml of counter-electrolyte was used for the 10% CO_2 feed, and 10 ml of counter-electrolyte was used for the 1% and 2,000 ppm CO_2 feeds. For 1% and 2,000 ppm CO_2 capture–release cycles, the sorbent tank was reduced at 10 mA for 1 h before running the cyclic test to reduce the oxidation overpotential.

flow rate. For over 15 capture–release cycles, the CO_2 concentration dropped from 10% to 2%, with a capacity utilization efficiency of ~60% (Fig. 8a,b and Supplementary Fig. 28). The minimum concentration achievable was limited by CO_2 transport across the gas–liquid interface, which can be enhanced by better contactor designs[45–47]. We also assessed CO_2 removal from low-concentration feeds. The system showed promising performance under 1% (Fig. 8c,d and Supplementary Fig. 29) and 2,000 ppm CO_2 (Fig. 8e,f and Supplementary Fig. 30). Both conditions showed stable operation over 15 cycles, with capacity utilization of ~80% and ~70%, respectively. The system kept outstanding stabilities under low CO_2 concentrations, showing near-unity Coulombic efficiencies and ~80% release/capture efficiencies. The average energy costs for 1% and 2,000 ppm CO_2 capture were 148.5 and 192.5 kJ per mol CO_2, respectively. Notably, the CO_2 concentration dropped to 0 in the 2,000 ppm experiment, indicating the high CO_2 affinity of the system and the possibility for direct air capture.

Finally, we found that glycol ethers such as diethylene glycol monomethyl ether can be employed as both sorbent and electrolyte solvent due to their sufficient salt-solubilizing ability (Supplementary Fig. 31). This opens future opportunities for co-designing liquid molecules with high CO_2 affinity, good electrolyte-forming capability, low volatility and low viscosity to further enhance the performance metrics.

Conclusions

In summary, we report an EMCC mechanism via non-aqueous PCET. The redox-tunable Brønsted basicity of organic molecules is utilized to reversibly deprotonate and regenerate alcohols, affording alkoxides and alkyl carbonates as the active sorbent and carbon capture product, respectively. This mechanism sidesteps the O_2 sensitivity issue of most EMCC mechanisms involving redox-active organic molecules, as all species involved in the process are intrinsically air stable. This work paves the way towards developing efficient carbon capture systems driven by electrochemical stimuli. Future material- and device-level designs, such as immobilizing redox-tunable bases on electrodes and spatially separating electrochemical reaction from absorption, provide abundant opportunities to further improve the EMCC performance.

Methods

Unless otherwise stated, all chemicals were purchased from commercial sources and used without further purification.

Characterizations

^{1}H NMR spectra were collected using a Bruker AMX400 (400 MHz) spectrometer at 300 K. ^{1}H NMR chemical shifts (δ) are given relative to tetramethylsilane, and residual solvent peaks were used as an internal reference for ^{1}H NMR spectra (DMSO: $\delta = 2.50$ ppm). Chemical shifts are reported in parts per million (ppm). The recycle delay (D1) was set to 1 s for all ^{1}H NMR experiments, with a subsequent acquisition time of 5.5 s. The number of scans is set as 32 for all ^{1}H NMR spectra to obtain strong signals. Attenuated total reflectance FTIR spectra were recorded on a ThermoNicolet iS5 spectrometer.

Electrochemical measurements

Electrochemical measurements such as cyclic voltammetry and chronoamperometry were conducted using a BioLogic VSP potentiostat with DMSO as the solvent and 0.1 M NBu_4PF_6 as the supporting salt unless otherwise specified. Glassy carbon ($Ø = 3$ mm) was used as the working electrode, a platinum wire was used as the counter-electrode, a silver wire was used as a pseudo-reference electrode and Fc was used as an internal reference. The electrolytes were purged with gases for 15 min (at a flow rate of 30 sccm) and stirred constantly before each measurement. After purging, the gas flow was maintained at the headspace of the electrolyte. Between consecutive measurements, the working electrode was polished, sonicated, rinsed with ethanol and dried completely. Typical CVs were collected at a scan rate of 20 mV s^{-1}.

Bulk electrolysis

Constant-current bulk electrolyses were carried out in non-deuterated DMSO to obtain the two-electron-reduced redox-tunable Brønsted bases for NMR characterizations. The set-up consisted of a flask with three necks for the working, counter- and reference electrodes. A piece of carbon felt (CT GF030, Fuel Cell Store) was used as the working electrode, lithium iron phosphate cast on carbon felt was used as the counter-electrode and a silver wire was used as the reference electrode. The counter-electrode was immersed in a neat electrolyte and separated from the bulk electrolysis solution with a fritted electrode chamber (MR-1196, Bioanalytical Systems). The three necks were sealed with rubber septa. The electrolyte solution was magnetically stirred and bubbled with CO_2 or N_2 during bulk electrolysis. To prepare the counter-electrode, lithium iron phosphate (MSE Supplies), polyvinylidene fluoride and carbon black (VULCAN XC72) were dispersed in chloroform at a mass ratio of 8:1:1, dropped onto carbon felt and dried on an 80 °C hotplate. Each electrode had a lithium iron phosphate loading of 70–80 mg. NMR samples were prepared by mixing 0.5 ml of electrolyte solution with 0.3 ml of deuterated DMSO.

Chemical preparation of alkoxides and phenoxides

Strong bases (sodium hydride and sodium hydroxide) were used to prepare alkoxides and phenoxides. To deprotonate linear alcohols, 3 ml of alcohol was injected into a 20 ml vial with a septum cap containing 0.024 g sodium hydride (60 wt% dispersed in mineral oil) using a 1 ml syringe. The reaction was carried out for 30 min to afford 0.2 M alkoxide dissolved in the corresponding alcohol. A similar procedure was conducted to deprotonate 2,6-substituted phenols, with the only difference being that the solid phenol species were first dissolved in DMSO (0.2 M solution) before being injected into the vial. To deprotonate 4-substituted phenols, phenol species were first dissolved in DMSO to obtain a 2 M solution. Subsequently, 0.5 ml of solution was injected into a 20 ml vial containing 0.5 ml of 2 M sodium hydride aqueous solution. After 10 min of reaction, 4 ml of DMSO was injected into the vial to obtain a final solution of 0.2 M 4-substituted phenoxide. The solutions were magnetically stirred and bubbled with N_2 during the chemical deprotonation process. All prepared solutions were used immediately for the injection experiments.

Chemical validation of CO_2 capture and release via injection experiments

In a typical experiment, a 20 ml vial with a septum cap containing 4 ml of DMSO was continuously purged with 20% CO_2 at a flow rate of 2 sccm controlled by a mass flow meter, and the outlet CO_2 concentration was recorded using an infrared-based sensor (GC-0121, GasLab). The sensor was calibrated using nitrogen and 20% CO_2 before each experiment. When the CO_2 sensor reading became stable, 0.45 ml of alkoxide/phenoxide solution was injected into the vial using a 1 ml syringe. The CO_2 response curve was integrated to determine the amount of CO_2 absorbed. The physical solubility of CO_2 was measured by injecting 0.45 ml of solvent (corresponding pure alcohol for linear alcohol, pure DMSO for 2,6-substituted phenols and a mixture of DMSO and water at a volume ratio of 9:1 for 4-substituted phenols), and the value was subtracted to determine the chemisorption capacity of alkoxides and phenoxides. The experiments for each species were performed in triplicate to obtain reliable quantification results.

Nafion membrane pretreatment

The Nafion membranes (Nafion 212 or 115, Chemours) were pretreated by first boiling the membrane in 3% hydrogen peroxide for 1 h. The membranes were then boiled in 0.25 M H_2SO_4 solution for 1 h and cleaned in boiling deionized water for 30 min (twice). Subsequently, the membranes were boiled in 0.25 M sodium hydroxide solution for 1 h and cleaned in boiling deionized water for 30 min (twice). Finally, the membranes were dried under vacuum at 80 °C overnight and stored in DMSO containing 0.25 M NaTFSI.

Flow cell set-up

In a typical experiment, the sorbent tank (20 ml scintillation vial with septum cap) was continuously bubbled with mixed gas with the flow rate controlled by a mass flow controller (Alicat Scientific). An infrared-based CO_2 sensor was connected at the gas exit to monitor the CO_2 concentration continuously. The Fc tank (20 ml scintillation vial with septum cap) was kept air free. The sorbent electrolyte consisted of 0.1 M AzB and 4 M *n*-butanol in DMSO with 0.25 M LiTFSI as the supporting salt. The counter-electrolyte contained 0.1 M Fc in DMSO with 0.25 M LiTFSI and 4 M *n*-butanol. A two-channel peristaltic pump (Ismatec Reglo ICC Digital Pump; Cole-Parmer) was used to circulate the sorbent and the Fc electrolytes into a commercial flow cell (Scribner) at a flow rate of 10 ml min^{-1}. The flow cell utilized graphite plates with 5 cm^2 or 25 cm^2 interdigitated flow fields pressed against two layers of carbon paper (Fuel Cell Store) to distribute the liquid flow. The carbon papers were held in place by Kalrez fluoropolymer elastomer gaskets (0.02 in. thick). A Nafion membrane (Nafion 115 for 10% CO_2 deep removal test and Nafion 212 for other tests) was placed between the carbon paper electrodes. Between the membrane and carbon paper electrodes, a layer of polypropylene separator (Celgard 3501) was placed to avoid short circuits.

Computational methods

All DFT calculations were performed using the Jaguar v.11.7 software by Schrödinger[48]. All calculations featured Truhlar's M06-2x functional[49] with Grimme's D3BJ empirical correction[50] for London dispersion forces. All atoms were described by Pople's triple-zeta 6-311G basis set[51] augmented with polarization and diffuse functions. The solvent environment was modelled via a Poisson–Boltzmann continuum based on Poisson–Boltzmann Finite element method[52] with parameters matching DMSO. Frequencies were computed to predict thermochemical properties such as enthalpies, zero-point energies and entropies. To account for librational modes hindered by the solvent environment, translational and rotational entropy modes were reduced by 50%. Note that we do not expect the presence of *n*-butanol to change the continuum properties of the implicit solvent. We expect the hydrogen bonding between *n*-butanol and reduced AzB to affect only the PCET kinetics, not the overall PCET thermodynamics (the latter being what we are interested in). In our calculations, we found that the inclusion of the hydrogen-bonded precomplex indeed alters the barrier for PCET but does not alter the global PCET thermodynamics.

Data availability

The data generated or analysed during this study are included in the published article and its Supplementary Information file. Source data are provided with this paper.

References

1. Lee, H. et al. *AR6 Synthesis Report. Summary for Policymakers* (IPCC, 2023).
2. Mac Dowell, N., Fennell, P. S., Shah, N. & Maitland, G. C. The role of CO_2 capture and utilization in mitigating climate change. *Nat. Clim. Change* **7**, 243–249 (2017).
3. Chu, S. Carbon capture and sequestration. *Science* **325**, 1599 (2009).
4. Bui, M. et al. Carbon capture and storage (CCS): the way forward. *Energy Environ. Sci.* **11**, 1062–1176 (2018).
5. Sanz-Pérez, E. S., Murdock, C. R., Didas, S. A. & Jones, C. W. Direct capture of CO_2 from ambient air. *Chem. Rev.* **116**, 11840–11876 (2016).
6. Rochelle, G. T. Amine scrubbing for CO_2 capture. *Science* **325**, 1652–1654 (2009).
7. Keith, D. W., Holmes, G., Angelo, D. S. & Heidel, K. A process for capturing CO_2 from the atmosphere. *Joule* **2**, 1573–1594 (2018).
8. Heldebrant, D. J. et al. Water-lean solvents for post-combustion CO_2 capture: fundamentals, uncertainties, opportunities, and outlook. *Chem. Rev.* **117**, 9594–9624 (2017).
9. Cantu, D. C. et al. Structure–property reduced order model for viscosity prediction in single-component CO_2-binding organic liquids. *Green Chem.* **18**, 6004–6011 (2016).
10. Heldebrant, D. J., Yonker, C. R., Jessop, P. G. & Phan, L. Organic liquid CO_2 capture agents with high gravimetric CO_2 capacity. *Energy Environ. Sci.* **1**, 487–493 (2008).
11. Jiang, Y. et al. Techno-economic comparison of various process configurations for post-combustion carbon capture using a single-component water-lean solvent. *Int. J. Greenh. Gas Control* **106**, 103279 (2021).
12. Ciferno, J. P., Fout, T. E., Jones, A. P. & Murphy, J. T. Capturing carbon from existing coal-fired power plants. *Chem. Eng. Prog.* **105**, 33 (2009).
13. Rheinhardt, J. H., Singh, P., Tarakeshwar, P. & Buttry, D. A. Electrochemical capture and release of carbon dioxide. *ACS Energy Lett.* **2**, 454–461 (2017).
14. Sharifian, R., Wagterveld, R. M., Digdaya, I. A., Xiang, C. & Vermaas, D. A. Electrochemical carbon dioxide capture to close the carbon cycle. *Energy Environ. Sci.* **14**, 781–814 (2021).
15. Renfrew, S. E., Starr, D. E. & Strasser, P. Electrochemical approaches toward CO_2 capture and concentration. *ACS Catal.* **10**, 13058–13074 (2020).
16. Diederichsen, K. M. et al. Electrochemical methods for carbon dioxide separations. *Nat. Rev. Methods Primers* **2**, 68 (2022).
17. Voskian, S. & Hatton, T. A. Faradaic electro-swing reactive adsorption for CO_2 capture. *Energy Environ. Sci.* **12**, 3530–3547 (2019).
18. Gurkan, B., Simeon, F. & Hatton, T. A. Quinone reduction in ionic liquids for electrochemical CO_2 separation. *ACS Sustain. Chem. Eng.* **3**, 1394–1405 (2015).
19. Diederichsen, K. M., Liu, Y., Ozbek, N., Seo, H. & Hatton, T. A. Toward solvent-free continuous-flow electrochemically mediated carbon capture with high-concentration liquid quinone chemistry. *Joule* **6**, 221–239 (2022).
20. Li, X., Zhao, X., Liu, Y., Hatton, T. A. & Liu, Y. Redox-tunable Lewis bases for electrochemical carbon dioxide capture. *Nat. Energy* **7**, 1065–1075 (2022).
21. Jeziorek, D. et al. Theoretical and electrochemical study of the mechanism of anthraquinone-mediated one-electron reduction of oxygen: the involvement of adducts of dioxygen species to anthraquinones. *J. Chem. Soc. Perkin Trans.* **2**, 229–236 (1997).
22. Liu, Y., Ye, H.-Z., Diederichsen, K. M., Van Voorhis, T. & Hatton, T. A. Electrochemically mediated carbon dioxide separation with quinone chemistry in salt-concentrated aqueous media. *Nat. Commun.* **11**, 2278 (2020).
23. Barlow, J. M. & Yang, J. Y. Oxygen-stable electrochemical CO_2 capture and concentration with quinones using alcohol additives. *J. Am. Chem. Soc.* **144**, 14161–14169 (2022).
24. Barlow, J. M. et al. Molecular design of redox carriers for electrochemical CO_2 capture and concentration. *Chem. Soc. Rev.* **51**, 8415–8433 (2022).
25. Schneider, C., Lafortune, J. H. W., Melen, R. L. & Stephan, D. W. Lewis and Brønsted basicity of phosphine–diazomethane derivatives. *Dalton Trans.* **47**, 12742–12749 (2018).
26. Voegtle, M. J. & Dawlaty, J. M. Can Brønsted photobases act as Lewis photobases? *J. Am. Chem. Soc.* **144**, 8178–8184 (2022).
27. Hammes-Schiffer, S. Theory of proton-coupled electron transfer in energy conversion processes. *Acc. Chem. Res.* **42**, 1881–1889 (2009).
28. Weinberg, D. R. et al. Proton-coupled electron transfer. *Chem. Rev.* **112**, 4016–4093 (2012).
29. Privalova, E. et al. CO_2 removal with 'switchable' versus 'classical' ionic liquids. *Sep. Purif. Technol.* **97**, 42–50 (2012).
30. Gupta, N. & Linschitz, H. Hydrogen-bonding and protonation effects in electrochemistry of quinones in aprotic solvents. *J. Am. Chem. Soc.* **119**, 6384–6391 (1997).
31. Katsumi, J., Nakayama, T., Esaka, Y. & Uno, B. Mechanistic study on the electrochemical reduction of 9,10-anthraquinone in the presence of hydrogen-bond and proton donating additives. *Anal. Sci.* **28**, 257–265 (2012).
32. Yang, Q. et al. Holistic prediction of the pK_a in diverse solvents based on a machine-learning approach. *Angew. Chem. Int. Ed.* **59**, 19282–19291 (2020).
33. Ugur, I., Marion, A., Parant, S., Jensen, J. H. & Monard, G. Rationalization of the pK_a values of alcohols and thiols using atomic charge descriptors and its application to the prediction of amino acid pK_a's. *J. Chem. Inf. Model.* **54**, 2200–2213 (2014).
34. Cheng, S. & Hawley, M. D. Electro-generated bases: the role of weak electroinactive proton donors and the effect of electrocatalysis on the redox behavior of azobenzene. *J. Org. Chem.* **50**, 3388–3392 (1985).
35. Suo, X. et al. CO_2 chemisorption behavior of coordination-derived phenolate sorbents. *ChemSusChem* **14**, 2854–2859 (2021).
36. Matsuta, S., Asada, T. & Kitaura, K. Vibrational assignments of lithium alkyl carbonate and lithium alkoxide in the infrared spectra an ab initio MO study. *J. Electrochem. Soc.* **147**, 1695–1702 (2000).
37. Gireaud, L., Grugeon, S., Laruelle, S., Pilard, S. & Tarascon, J. M. Identification of Li battery electrolyte degradation products through direct synthesis and characterization of alkyl carbonate salts. *J. Electrochem. Soc.* **152**, A850 (2005).
38. Zhang, Z., Kummeth, A. L., Yang, J. Y. & Alexandrova, A. N. Inverse molecular design of alkoxides and phenoxides for aqueous direct air capture of CO_2. *Proc. Natl Acad. Sci. USA* **119**, e2123496119 (2022).
39. Lehmann, M. L. et al. Membrane design for non-aqueous redox flow batteries: current status and path forward. *Chem* **8**, 1611–1636 (2022).

40. Pezeshki, A. M., Clement, J. T., Veith, G. M., Zawodzinski, T. A. & Mench, M. M. High performance electrodes in vanadium redox flow batteries through oxygen-enriched thermal activation. *J. Power Sources* **294**, 333–338 (2015).
41. Seo, H. & Hatton, T. A. Electrochemical direct air capture of CO_2 using neutral red as reversible redox-active material. *Nat. Commun.* **14**, 313 (2023).
42. Pang, S. et al. A phenazine-based high-capacity and high-stability electrochemical CO_2 capture cell with coupled electricity storage. *Nat. Energy* **8**, 1126–1136 (2023).
43. Jin, S., Wu, M., Jing, Y., Gordon, R. G. & Aziz, M. J. Low energy carbon capture via electrochemically induced pH swing with electrochemical rebalancing. *Nat. Commun.* **13**, 2140 (2022).
44. Jin, S., Wu, M., Gordon, R. G., Aziz, M. J. & Kwabi, D. G. pH swing cycle for CO_2 capture electrochemically driven through proton-coupled electron transfer. *Energy Environ. Sci.* **13**, 3706–3722 (2020).
45. Diederichsen, K. M. & Hatton, T. A. Nondimensional analysis of a hollow fiber membrane contactor for direct air capture. *Ind. Eng. Chem. Res.* **61**, 11964–11976 (2022).
46. Diederichsen, K. M., Dewitt, S. J. A. & Hatton, T. A. Electrochemically facilitated transport of CO_2 between gas diffusion electrodes in flat and hollow fiber geometries. *ACS EST Eng.* **3**, 1001–1012 (2023).
47. Chuah, C. Y., Kim, K., Lee, J., Koh, D.-Y. & Bae, T.-H. CO_2 absorption using membrane contactors: recent progress and future perspective. *Ind. Eng. Chem. Res.* **59**, 6773–6794 (2020).
48. Bochevarov, A. D. et al. Jaguar: a high-performance quantum chemistry software program with strengths in life and materials sciences. *Int. J. Quantum Chem.* **113**, 2110–2142 (2013).
49. Zhao, Y. & Truhlar, D. G. The M06 suite of density functionals for main group thermochemistry, thermochemical kinetics, noncovalent interactions, excited states, and transition elements: two new functionals and systematic testing of four M06-class functionals and 12 other functionals. *Theor. Chem. Acc.* **120**, 215–241 (2008).
50. Grimme, S., Antony, J., Ehrlich, S. & Krieg, H. A consistent and accurate ab initio parametrization of density functional dispersion correction (DFT-D) for the 94 elements H–Pu. *J. Chem. Phys.* **132**, 154104 (2010).
51. Hehre, W. J., Ditchfield, R. & Pople, J. A. Self-consistent molecular orbital methods. XII. Further extensions of Gaussian-type basis sets for use in molecular orbital studies of organic molecules. *J. Chem. Phys.* **56**, 2257–2261 (1972).
52. Tannor, D. J. et al. Accurate first principles calculation of molecular charge distributions and solvation energies from ab initio quantum mechanics and continuum dielectric theory. *J. Am. Chem. Soc.* **116**, 11875–11882 (1994).

Acknowledgements

We acknowledge financial support from the Johns Hopkins University (A.L., X.L., Y.L.), the National Science Foundation (award 2237096, A.L., Y.L.) and the David and Lucile Packard Foundation (A.L., Y.L.). C.B.M. and W.A.G. acknowledge support from the Liquid Sunlight Alliance, which is supported by the US Department of Energy, Office of Science, Office of Basic Energy Sciences, Fuels from Sunlight Hub under award DE-SC0021266. This research used resources of the National Energy Research Scientific Computing Center, a DOE Office of Science User Facility supported by the Office of Science of the US Department of Energy under contract DE-AC02-05CH11231 using NERSC award BES-ERCAP0024109 (C.B.M., W.A.G.).

Author contributions

Y.L. conceived the project and designed the experiments. A.L. and X.L. conducted the experiment and analysed the data. C.B.M. performed the DFT calculations under the supervision of W.A.G. Y.L. supervised the project. A.L. and Y.L. co-wrote the paper. All authors discussed the results and revised or commented on the paper.

Competing interests

The authors declare no competing interests.

Additional information

Supplementary information The online version contains supplementary material available at https://doi.org/10.1038/s41560-024-01614-7.

Correspondence and requests for materials should be addressed to Yayuan Liu.

Peer review information *Nature Energy* thanks the anonymous reviewers for their contribution to the peer review of this work.

Reprints and permissions information is available at www.nature.com/reprints.